Nanoscale

ROYAL SOCIETY OF CHEMISTRY

PAPER

View Article Online
View Journal | View Issue

Cite this: *Nanoscale*, 2024, **16**, 19881

Multivalent nanobody engineering for enhanced physisorption and functional display on gold nanoparticles†

John-Paul Ayrton, [a,b] Chapman Ho, [a,b] Haoran Zhang,[b] Vijay Chudasama, [c] Stefanie Frank *[b] and Michael R. Thomas *[a,b]

The ease of expression and engineering of single domain antibodies, known as nanobodies, make them attractive alternatives to conventional antibodies in point-of-care diagnostics such as lateral flow assays. In lateral flow assays, gold nanoparticle bioconjugates serve as labels which display affinity molecules on the gold surface. While examples of nanobody gold nanoparticle bioconjugates exist, few utilise the simple one-step approach of physisorption owing to undesirable nanoparticle aggregation and loss of functionality. Here we show that engineering nanobodies into multivalent structures can significantly enhance their functionality when physisorbed onto gold nanoparticles. This approach enables resulting bioconjugates to withstand multiple processing steps required for long-term nanoparticle storage within lateral flow assays. Specifically, we show that the trivalent version of VHHV nanobody (VHH3) against the S1 protein of SARS-CoV-2 can be immobilised onto gold nanoparticles through passive adsorption. Unlike its monovalent and bivalent nanobody counterparts, using VHHV3 preserves nanoparticle stability under salt stress, blocking, washing, and freeze-drying conditions while maintaining picomolar sensitivity to the S1 protein. We anticipate that this facile strategy is a significant advancement towards the integration of nanobodies in lateral flow assay development.

Received 3rd July 2024,
Accepted 27th September 2024

DOI: 10.1039/d4nr02762k

rsc.li/nanoscale

Introduction

The COVID-19 pandemic exposed a critical need for rapid, accessible diagnostics to combat emerging infectious diseases.[1] Real-time information from widespread testing is essential for enabling effective responses, such as contact tracing and isolation, particularly when considering the longer timelines associated with vaccine and therapeutic pipelines.[2,3] The development of traditional antigen lateral flow assays (LFA) is a complex iterative process that fundamentally relies on the availability of suitable antibody pairs which meet the sensitivity and specificity requirements for the target disease.[4] Although monoclonal antibodies have been widely implemented in LFAs, their costly and complex development process represents a bottleneck in LFA development.[5]

Nanobodies, fragments of heavy chain-only antibodies found in camelids, offer unique advantages over traditional antibodies in the realm of diagnostics.[6] Their amenability to phage display platforms and the ability for synthetic generation from immune libraries has been shown to enable the development of sub-nanomolar affinity binders in as little as 3 weeks.[7,8] More recently, developments in de-novo binder design have enabled the generation of functional nanobodies with no reliance on animal use.[9] Nanobodies can be easily produced in bacteria with exceptional titres, unlike traditional antibody production which necessitates costly mammalian cell cultures.[10–12] This simplified expression in bacteria not only accelerates production significantly, but also enables a more decentralised production model, empowering research groups, diagnostic companies, and even local manufacturers in resource-limited settings to produce their own nanobody-based tools, fostering a globally accessible and responsive diagnostic ecosystem. Furthermore, nanobodies benefit from a greater chance of a nanobody pair hit due to their smaller size, ability to access cryptic epitopes that are less susceptible to mutational escape and exhibit exceptional physical stability properties.[13]

The development of gold nanoparticle (AuNP) bioconjugates is a crucial step in the LFA development process.

[a]*London Centre for Nanotechnology, University College London, London, UK. E-mail: michael.thomas@ucl.ac.uk*
[b]*Department of Biochemical Engineering, University College London, London, UK. E-mail: stefanie.frank@ucl.ac.uk*
[c]*Department of Chemistry, University College London, London, UK*

† Electronic supplementary information (ESI) available. See DOI: https://doi.org/10.1039/d4nr02762k

Proteins can be chemically attached to gold nanoparticles by exploiting functional groups such as thiols or amines, or be physically adsorbed to the surface by electrostatic interactions through charged and hydrophobic residues.[14] While amines can be targeted with carbodiimide crosslinkers, thiols (found in cysteine residues) can be targeted with thiol reactive cross linkers or directly coupled to a gold surface through a dative covalent bond.[15–17] Nanobodies, with their unique properties, are emerging as compelling affinity reagents for diagnostics and nanoparticle conjugation.[18–21] Their smaller size, compared to conventional antibodies, holds promise for increasing coating density on sensor surfaces which is linked to improvement in analytical performance.[22] While various nanobody bioconjugation chemistries exist, including click chemistry, *N*-hydroxysuccinimide (NHS) and maleimide pre-activated kits, SpyTag/SpyCatcher mediated and site-specific biotinylation, passive adsorption offers a simple, cost-effective, and scalable approach.[23–27] However, as highlighted by Goossens *et al.*, nanobody-gold nanoparticle (AuNP) bioconjugates generated through passive adsorption can face challenges resulting from nanoparticle aggregation.[28] Nanoparticle stability also represents a pressing issue for LFA bioconjugates, given that LFAs are prized for their storability in ambient conditions and must therefore withstand multiple processing steps, including blocking, washing, and drying.

Protein engineering strategies have been previously explored to improve nanobody AuNP physisorption. Hattori *et al.* developed a novel anti-gold nanobody which, upon physisorption onto 20 nm AuNPs, maintained a degree of resistance to elevated ionic strengths.[29] They demonstrated the feasibility of a bispecific nanobody approach to promote particle assembly, where one nanobody (anti-gold nanobody) facilitated immobilisation while the other provided biorecognition of a secondary particle. However, while their gold binding nanobody was able to form bioconjugates, complete suppression of salt-induced aggregation was not achieved under all tested conditions. Goossens *et al.* employed a similar bispecific construct incorporating the same anti-gold nanobody but found this did not prevent the aggregation of 20 nm AuNP bioconjugates. Additionally, they conjugated a series of nanobodies to AuNPs in their native form through physisorption. While this approach generated functional nanobody-AuNP bioconjugates, the results showed varying degrees of susceptibility to salt induced aggregation across different nanobodies. Furthermore, they explored dative covalent bond-mediated immobilisation using cysteine-bearing nanobodies, but again, this was not found to improve nanoparticle stability.[28] Notably, the bioconjugates were prone to aggregation in the presence of blocker proteins, a critical factor for LFA applications since the bioconjugates are required to interface with common blocking proteins such as bovine serum albumin (BSA), and complex sample matrices. In contrast, Anderson *et al.* investigated various nanobody modifications, including fusion with metal-binding peptides and cysteine-bearing peptides.[30] They found that incorporating a cysteine-bearing tag (hop-tail) was the optimal strategy for enhancing bioconjugate stability compared to native nanobody constructs although at the cost of additional reduction steps in the production of AuNP bioconjugates. To date, these studies have involved the use of bioconjugates prepared and stored in the liquid phase, leaving the impact of harsher processes, such as drying, on the stability of bioconjugates unknown.

In this study, we demonstrate the importance of engineering multivalent nanobodies to enhance bioconjugate stability and performance in LFAs. Initially, we investigated the physisorption characteristics of 3 different nanobodies of varied isoelectric points (IEPs) against the SARS-CoV-2 S1 protein. In doing so, we further show the limitations of native nanobody physisorption and terminal-cysteine modifications on yielding colloidally stable bioconjugates *via* physisorption. To address this challenge, we introduced a rational protein engineering approach, incorporating the lead nanobody candidate into multivalent nanobody chains. Notably, a trivalent nanobody demonstrated superior analytical performance and enhanced nanoparticle stability under elevated osmotic strength conditions. The resulting trivalent nanobody bioconjugate is also shown to be resilient to the presence of blocker proteins encountered during bioconjugate processing and drying stages while maintaining picomolar-level detection of the S1 protein in a LFA format.

Results and discussion

Limits of nanobody-mediated protection against salt-induced AuNP aggregation

The bioconjugation of immunoglobulin antibodies to citrate-capped AuNPs typically occurs at a pH that is slightly more basic than the antibody's isoelectric point.[31,32] This enables a subtle, yet favourable electrostatic attraction between positively charged residues on the antibodies and negatively charged AuNPs. The electrostatic force of attraction must be strong enough to promote binding, but not so strong that it overcomes the electrostatic repulsion between individual AuNPs, which would lead to bridging and aggregation.[28] In the present study, recognising that nanobody diversity in charge and sequence can influence nanobody-AuNP interactions, we selected three nanobodies against the SARS-CoV-2 S1 protein. Nanobodies VHHV, VHHE, developed by Koenig *et al.*, and Nb6, developed by Schoof *et al.*, spanning a range of IEPs (6.70–9.39) were selected to probe how each undergo physisorption to AuNPs at different pHs (Fig. 1a).[8,33] Furthermore, nanobodies with low dissociation constants, indicative of high affinity for their target antigen, were selected to enhance their diagnostic potential and enable an assessment of the resulting bioconjugate's analytical performance. The selected nanobodies were expressed in *E. coli* and purified using nickel-nitrilotriacetic acid (Ni-NTA) affinity chromatography to yield purified nanobodies.

The physisorption of the 3 nanobodies to AuNPs was evaluated as a function of pH using a molar excess of 3200 nanobodies per nanoparticle. Given the dimensions of a typical nanobody (4 nm × 2.5 nm), and the surface area of a 40 nm gold

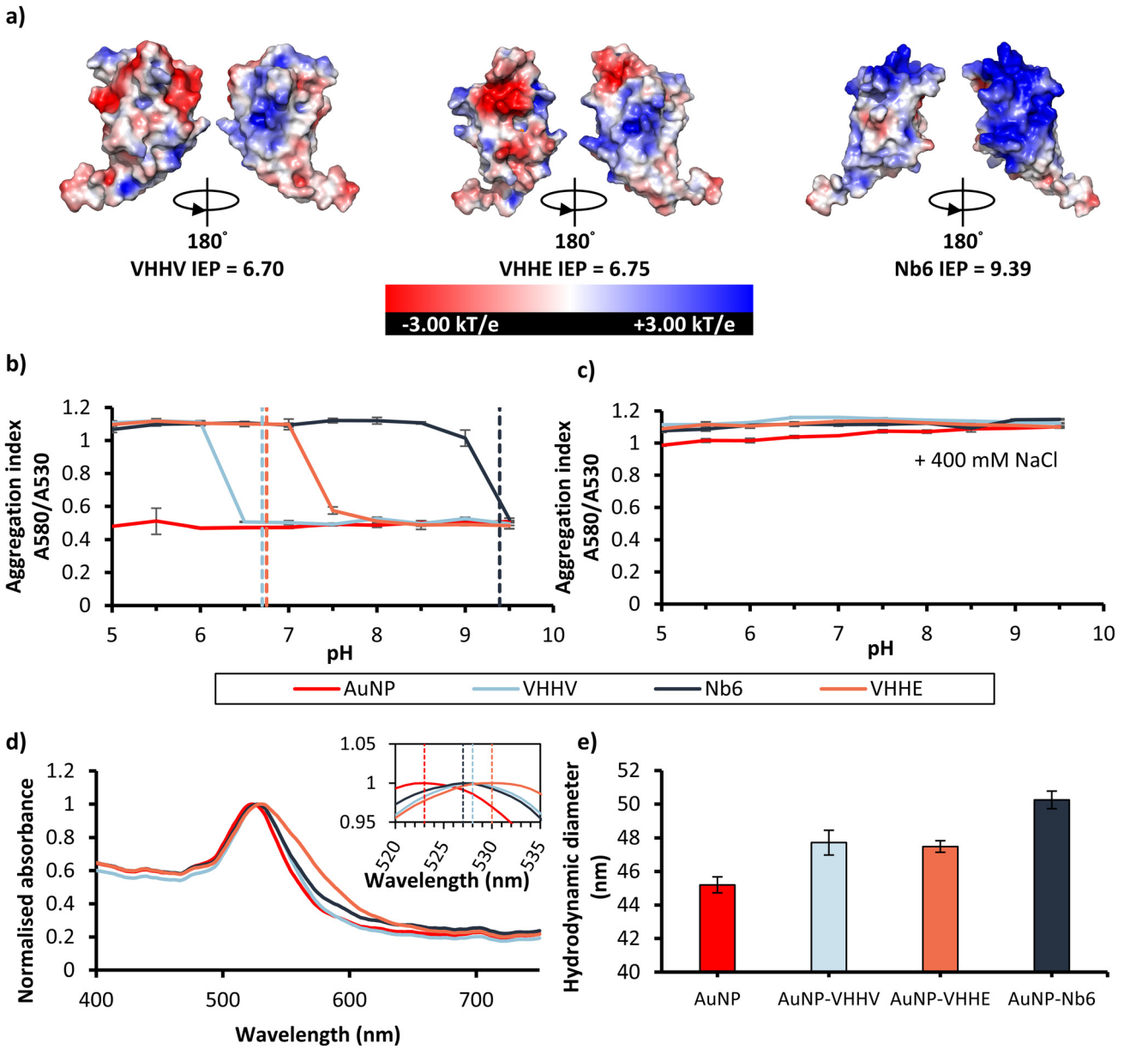

Fig. 1 Adsorption characteristics of anti-SARS-CoV-2 nanobodies on AuNPs. (a) Surface charge distribution of the 3 nanobodies, blue represents positive potential and red represents negative potential from $-3kT/e$ to $+3kT/e$ at pH 7. Surface and IEP calculations were performed using the APBS biomolecular solvation.[47] Nanobody 3D structures predicted by AlphaFold 2 using the accessible colabfold server.[48,49] (b) Aggregation index plots for each nanobody conjugation across a range of pH conditions. Dashed lines represent the IEP for each nanobody. Values are shown as the average (n = 3) and error bars indicate the standard deviation of the mean. (c) Aggregation index plots for each nanobody after increasing the NaCl concentration to 400 mM. Values are shown as the average (n = 3) and error bars indicate the standard deviation of the mean. (d) UV-Vis spectra of each nanobody bioconjugation reaction at the first stable pH condition for nanobodies VHHV (pH 6.5), VHHE (pH 7.5) and Nb6 (pH 9.5). Dashed lines in the subplot show the position of the plasmon peak. (e) Hydrodynamic diameter (D_h) of bare AuNP and for each nanobody bioconjugate immediately following physisorption. Values are shown as the average (n = 3) and error bars indicate the standard deviation of the mean.

nanoparticle (AuNP), we estimated that a close packed monolayer would require approximately 500 to 800 nanobodies, depending on their orientation on the surface.[34] In this regard, an excess ratio was used to ensure sufficient availability of nanobodies per AuNP, and favour binding of the nanobodies to the nanoparticle surface. Localised surface plasmonic resonance (LSPR) peak wavelengths were measured using UV-Vis to probe transitions from stable to unstable states. Loss in the intensity and broadening of the LSPR peak is indicative of nanoparticle aggregation. Aggregation can be quantified using an aggregation index (A530/580), defined as the ratio of the absorbance at the plasmon peak to the absorbance at the plasmon shoulder of 530 nm and 580 nm for 40 nm AuNPs, respectively.[32]

A strong physisorption pH dependence was identified for each nanobody during nanobody-AuNP bioconjugate formation (Fig. 1b). At low ionic strengths (10 mM), nanobody-AuNP bioconjugates with an A530/580 approaching 0.5 could be produced at defined pH ranges, indicating stable AuNPs. Using the most acidic nanobody VHHV (IEP = 6.70), physisorption yielded stable bioconjugates at pH conditions above 6.5 and aggregated conjugates below pH 6.5. The most basic nanobody Nb6 (IEP = 9.39) yielded stable bioconjugates at pH greater than 9.5. Nanobody VHHE (IEP = 6.75), however, required comparatively elevated pH conditions (pH > 7.5) in order to obtain stable bioconjugates. Increasing the molar excess of nanobodies VHHV and Nb6 to 9600 per nanoparticle showed no difference in bioconjugate stability suggesting that maximal modification had been achieved (ESI Fig. 1a and e†). On the contrary, increasing nanobody VHHE molar excess proved detrimental to nanoparticle stability as nanoparticle aggregation was observed across a broader pH range (ESI Fig. 1b†). This loss of stability at higher nanobody excess could indicate VHHE–VHHE interactions resulting in nanoparticle bridging and aggregation. To test this, a homologous sandwich ELISA format in the absence of the antigen composed of VHHE being both the detection and capture nanobody was performed (ESI Fig. 2†). An interaction of VHHE with itself was observed, indicating the potential for VHHE to cause nanoparticle bridging and aggregation during physisorption experiments *via* protein–protein interactions.

The physisorption process was further analysed using two approaches: the emergence of a redshift in the LSPR maximum resulting from local dielectric changes on protein binding to AuNPs, and the stability of the bioconjugates to elevated salt concentrations. The immobilisation of all 3 nanobodies onto AuNPs was found to result in a subtle redshift of about 5 nm as observed by UV-Vis spectroscopy, consistent with modification of the nanoparticle surface by protein (Fig. 1d).[35] While a protein monolayer may exist on the AuNP bioconjugate, this does not necessarily mean the nanoparticle is sufficiently stable to operate within the conditions of a LFA. The bioconjugates were therefore tested for stability by increasing the ionic strength of the solution through the addition of 400 mM NaCl. High ionic strengths cause a shortening of the length of the electric double layer between two approaching bioconjugates, which is crucial for maintaining the colloidal stability. If the surface has been sufficiently covered by protein, the colloid can be protected from salt-induced aggregation since the protein layer creates a steric, charged barrier around the nanoparticles, preventing the electron dense gold from directly contacting each other *via* van der Waals interactions.[36] As shown in Fig. 1c, physisorbed nanobodies do not prevent the salt-induced aggregation observed for bare AuNPs, consistent with previous findings.[28] Dynamic light scattering (DLS) was used to characterise the nanobody layer formed through bioconjugation by measuring changes in hydrodynamic diameter (D_h) compared to bare AuNPs. An increase in hydrodynamic diameter was noted post-bioconjugation with VHHV (47.7 nm ± 0.7), VHHE (47.5 nm ± 0.3), and Nb6 (50.2 nm ± 0.5) compared to bare gold nanoparticles (45.2 nm ± 0.5), confirming surface modification. However, given the dimensions of each nanobody, shown in Table 1, determined from the Protein Data Bank structures (ESI Fig. 3†), the calculated diameter changes for each bioconjugate post-physisorption fall short of the expected changes following the formation of a protein monolayer. The values obtained by DLS suggest that the nanoparticles are either not fully covered by nanobodies or that nanobodies unfold upon binding to the particle surface.

The smaller size of nanobodies, compared to larger IgG antibodies, may limit their ability to maintain the colloidal stability of AuNPs upon physisorption since they provide comparatively less steric repulsion at the particle surface. In addition to the insufficient steric repulsion offered by nanobodies, proteins are, in general, prone to unfolding on nanoparticle surfaces, further contributing to aggregation.[37,38] In subsequent sections, we investigate the incorporation of two strategies towards promoting nanobody-AuNP binding: free cysteines inserted into the VHHV nanobody construct and the generation of multivalent nanobody structures. These strategies aim to increase loading density and create a more robust protein layer on AuNP bioconjugates.

Generation of cysteine-bearing nanobodies

Proteins can form stable bonds with AuNPs through the thiol groups of cysteine residues.[39] While nanobodies typically contain pairs of cysteines, these are tied-up in disulfide bridges and are thus inaccessible for protein anchoring. To enhance the stability of nanobody-AuNP bioconjugates towards elevated ionic strength, a strategy for linking the nanobodies covalently to the surface was employed instead of only relying to electrostatic forces. To achieve this, we engineered cysteines on one of the nanobodies. The VHHV nanobody was chosen for the generation of the Cys-bearing nanobodies since VHHV-AuNP displayed the greatest stability over the broadest range of pH at low ionic strengths of the nanobodies studied. Two cysteine-bearing VHHV nanobodies were created with cysteine residues at different positions to study the influence of both the presence and location of the free thiols on bioconjugate stability. VHHV-Cys presented a cysteine on the C-terminus, distal to the paratope and after the hexahistidine purification tag, while Cys-VHHV presented a cysteine at the N-terminus.

While protein engineering offers powerful tools for tailoring protein function, it can also introduce unintended consequences such as misfolding and reduced affinity. The presence of free cysteines in engineered proteins like nanobodies can

Table 1 Nanobody dimensions

Nanobody	Dimensions (nm)	Measured change in AuNP diameter (nm)
VHHV	4.68 × 3.29 × 2.64	2.52
VHHE	5.36 × 3.29 × 3.60	2.29
Nb6	4.35 × 3.47 × 2.89	5.05

lead to dimerisation through the formation of inter-protein disulfide bridges, since they are expressed in the oxidative conditions of the bacterial periplasm. To assess this potential issue, we performed SDS-PAGE analysis under non-reducing conditions. As expected, VHHV showed a single band corresponding to the expected molecular weight of 14.23 kDa (Fig. 2b). In contrast, Cys-VHHV and VHHV-Cys exhibited both the monomeric band and a heavier band consistent with dimer formation. Treatment with 10 mM TCEP–HCl, a mild reducing agent, readily converted the dimers back to monomers (Fig. 2a and b) as previously shown.[40] The reduction reaction also carries the risk of reducing the internal disulfide bridge which could impact functionality, protein stability and the creation of further unintended binding sites that could complicate binding to the AuNP.

We employed liquid chromatography-mass spectrometry (LC-MS) to verify both the reduction of the dimerised VHHV-Cys construct to its monomeric form and the integrity of its internal disulfide bond. Prior to analysis, VHHV-Cys was reduced with TCEP–HCl and the reaction was quenched using the thiol-reactive reagent *N*-methylmaleimide (NMM). The presence of a single peak corresponding to the molecular weight of one VHHV-Cys molecule bound to a single NMM molecule indicated successful dimer reduction (ESI Fig. 4†). Additionally, this result confirmed the integrity of the internal disulfide bond, as its reduction would have resulted in mass additions that would reflect multiple free sulfhydryl groups reacting with NMM. To investigate potential functional changes caused by the cysteine addition or subsequent TCEP reduction process, we compared the analytical performance of VHHV, VHHV-Cys, and Cys-VHHV in an enzyme linked immunosorbent assay (ELISA) format. Reduced and non-reduced versions of each nanobody were immobilised on polystyrene plates, and limit of detection (LoD) analysis was conducted using a chemically biotinylated S1 protein. The amine reactive crosslinker NHS-PEG_{12}-Biotin was used to functionalise the S1 protein with biotin enabling the use of streptavidin-HRP for signal generation. We observed no significant differences in LoD between non-reduced and reduced versions of VHHV, VHHV-Cys, and Cys-VHHV (denoted as rVHHV, rVHHV-Cys and rCys-VHHV respectively). Intriguingly, rVHHV-Cys and rCys-VHHV demonstrated significantly improved LoD compared to the non-Cys bearing rVHHV (Fig. 2c). While rVHHV exhibited a LoD of 167 pM (110–252 pM, 95% CI), rVHHV-Cys and rCys-VHHV showed LoDs of 31.8 pM (19.9–50.0 pM, 95% CI) and 64.9 pM (23.0–177 pM, 95% CI), respectively. Although the origin of the effect is unclear, the results suggest that the free sulfhydryl group may facilitate an improvement of the nanobody as a capture affinity reagent in direct ELISA format, warranting further investigation.

Physisorption of cysteine-bearing nanobodies

To investigate the impact of cysteine modification on bioconjugate formation and stability, VHHV, VHHV-Cys and Cys-VHHV were conjugated to AuNPs at varied pH at a ratio of 3200 nanobodies per nanoparticle, consistent with earlier native nanobody experiments. Their stability before and after 400 mM NaCl addition was assessed by monitoring the aggregation index. These measurements were performed for both reduced

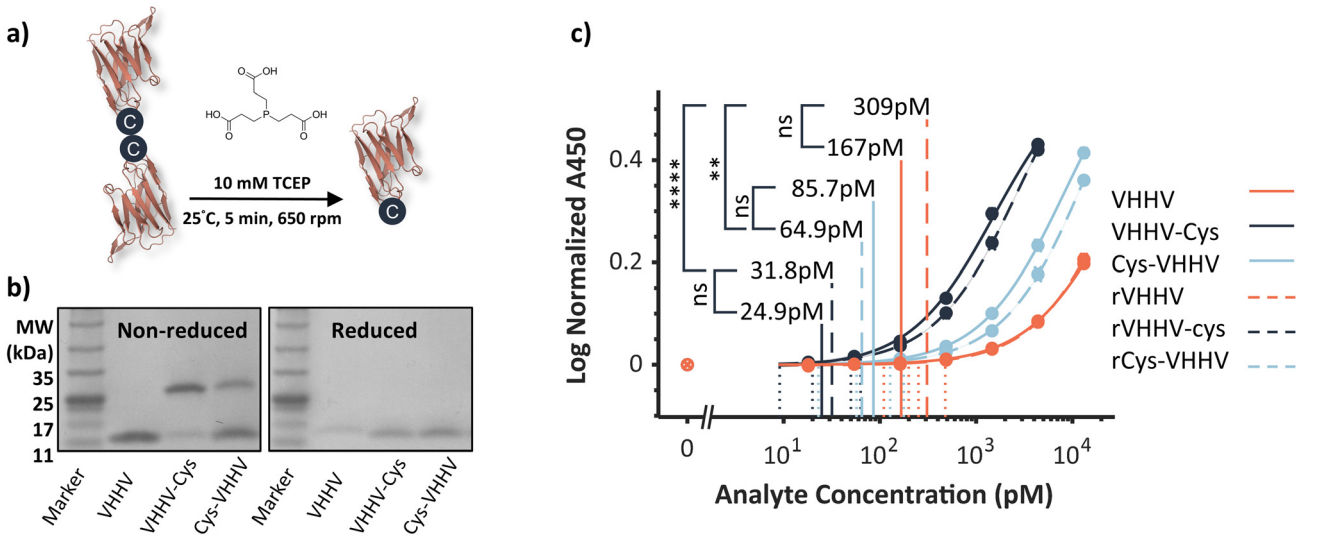

Fig. 2 Cys-nanobody reduction and characterisation. (a) Schematic showing the reduction of the dimerised nanobody to the monomer using TCEP–HCL. (b) SDS-PAGE showing the profile under non-reducing conditions before (left) and after reaction with TCEP–HCL (right). (c) Concentration–response curves for native and cysteine-bearing nanobodies (reduced and non-reduced) as ELISA capture reagents for biotinylated SARS-CoV-2 S1 protein. Dashed lines: fitted Langmuir functions for reduced nanobodies (VHHV, VHHV-Cys, Cys-VHHV) with limits of detection Solid lines: fitted Langmuir functions for non-reduced nanobodies with limits of detection. Solid circles show the mean value for each point (n = 3) while dotted lines show the 95% confidence intervals for each series. Significance was calculated using a two tailed t-test and denoted as ns – $p > 0.05$, **$p < 0.01$, ****$p < 0.001$.

(rVHHV, rVHHV-Cys, rCys-VHHV) and non-reduced versions of each nanobody to assess the impact of any dimerisation on the non-reduced nanobodies. Initially, the pH-dependent aggregation index profiles for both reduced and non-reduced cysteine-modified VHHV nanobodies exhibited a similar response to the unmodified VHHV. Nanoparticles were stable at pH values above the protein's isoelectric point (6.70) and aggregated below it (Fig. 3a). Successful immobilisation of nanobodies onto AuNPs was indicated by comparable plasmon shifts of approximately 5 nm for all VHHV variants (Fig. 3b). However, across all the nanobody cysteine variants, elevated salt concentrations were deleterious towards colloidal stability, leading to particle aggregation across all tested pH conditions (Fig. 3c).

Interestingly, only the non-reduced VHHV-Cys nanobody displayed enhanced colloidal stability and some resistance to salt-induced aggregation. In Fig. 2b, we identified a fraction of VHHV-Cys and Cys-VHHV in the dimerised form on SDS-PAGE. In the case of VHHV-Cys, the dimer fraction was the dominant fraction suggesting that nanobody dimerisation could influence particle stabilisation. This observation is consistent with our initial hypothesis that the nanobody, in its native form, may not provide sufficient protection against nanoparticle aggregation due to its small size, while the dimerised version shows some improvement in stability at higher pH. Despite this, DLS measurements revealed comparable increases in D_h for all VHHV variants (Fig. 3d). This may indicate that there is an influence of the proteins approaching as a pre-formed dimer, or of the disulfide linkage itself, with its tendency to bind Au, influencing the particle stability.

Generation and characterisation of multivalent nanobodies

In the previous section, the non-reduced cysteine derivative VHHV-Cys, presenting predominantly in dimerised form, exhibited improved stability to elevated ionic strength and pH. The approach of engineering a larger protein structure to physisorb at the AuNP surface provided an opportunity to target a thicker protein corona. A strategy was therefore devised to engineer nanobodies into multivalent states, a strat-

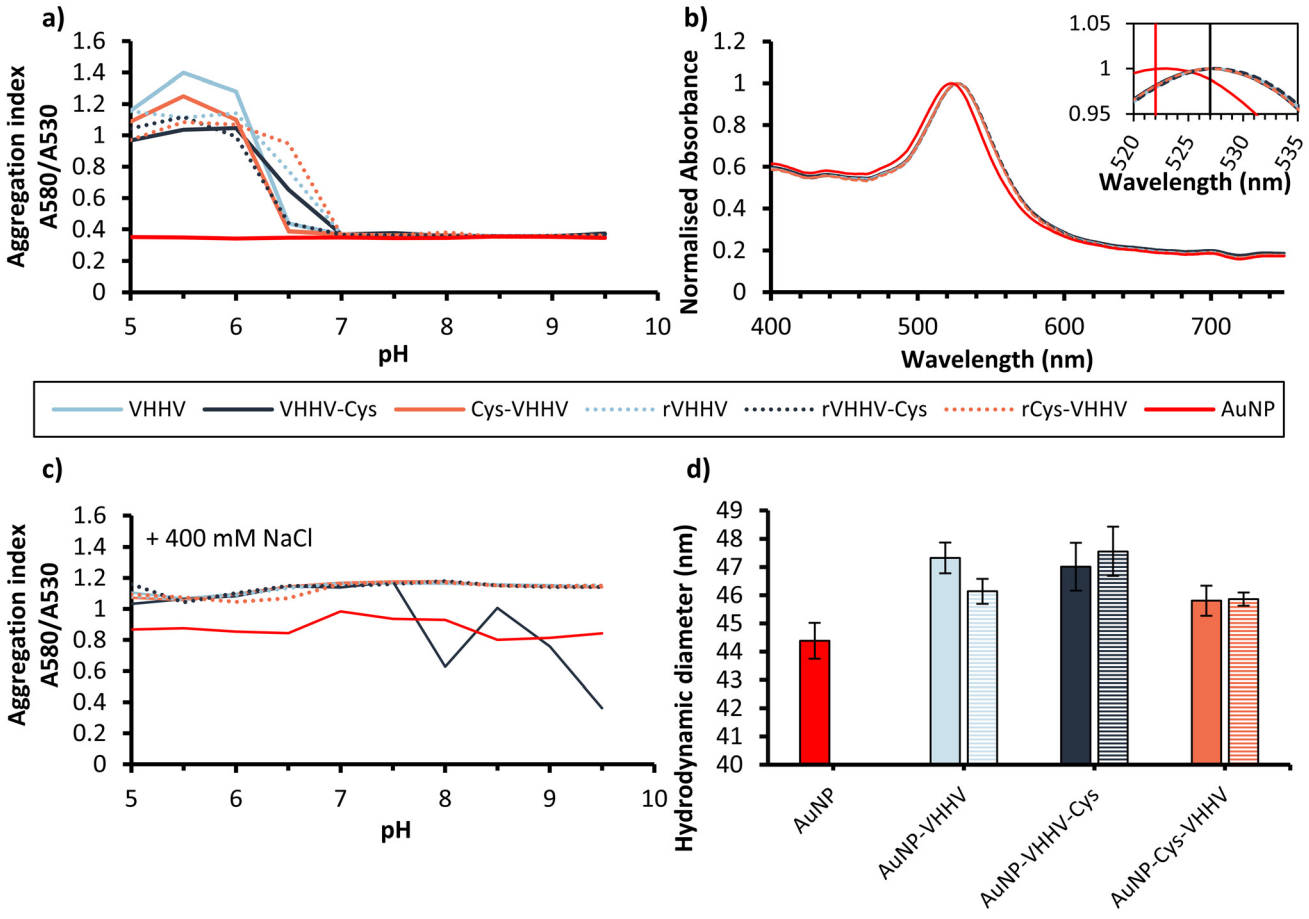

Fig. 3 AuNP adsorption characteristics of VHHV and cysteine bearing VHHV. Aggregation index plots for each Cys-nanobody conjugation across a range of pH conditions before (a) and after (c) increasing NaCl concentration to 400 mM. Reduced and non-reduced versions of each nanobody is represented by dashed and solid lines, respectively. (b) UV-Vis plot for Cys-nanobody bioconjugates. (d) Hydrodynamic diameter of bare AuNP and bioconjugates made from the reduced (dashed fill) and non-reduced (solid fill) versions of VHHV, VHHV-Cys and Cys-VHHV determined by DLS immediately following physisorption. Values are shown as the average (n = 3) and error bars indicate the standard deviation of the mean.

egy recently used to enhance binding to SARS-CoV-2 in neutralisation studies.[33,41] Multivalent nanobody chains, including a bivalent (VHHV2) and trivalent (VHHV3) nanobody, were generated with each nanobody domain linked by flexible GGGGS × 3 spacers as shown in Fig. 4a.

The binding properties of the nanobody constructs were initially studied using bio-layer interferometry (BLI) to reveal the associative and dissociative rates of the constructs against the S1 protein. BLI was performed with streptavidin-functionalised sensors and chemically biotinylated versions of each nanobody (VHHV, VHHV2, and VHHV3). Nanobodies were chosen to be loaded on the sensor instead of the antigen to reduce the chance of avidity effects caused by the binding of the multivalent structures to multiple antigens on the sensor. The chemical biotinylation of each nanobody was performed under identical stoichiometries to minimise heterogeneity in biotinylation load using the amine reactive NHS-PEG_{12}-Biotin linker. LC-MS analysis revealed a distribution of biotinylation

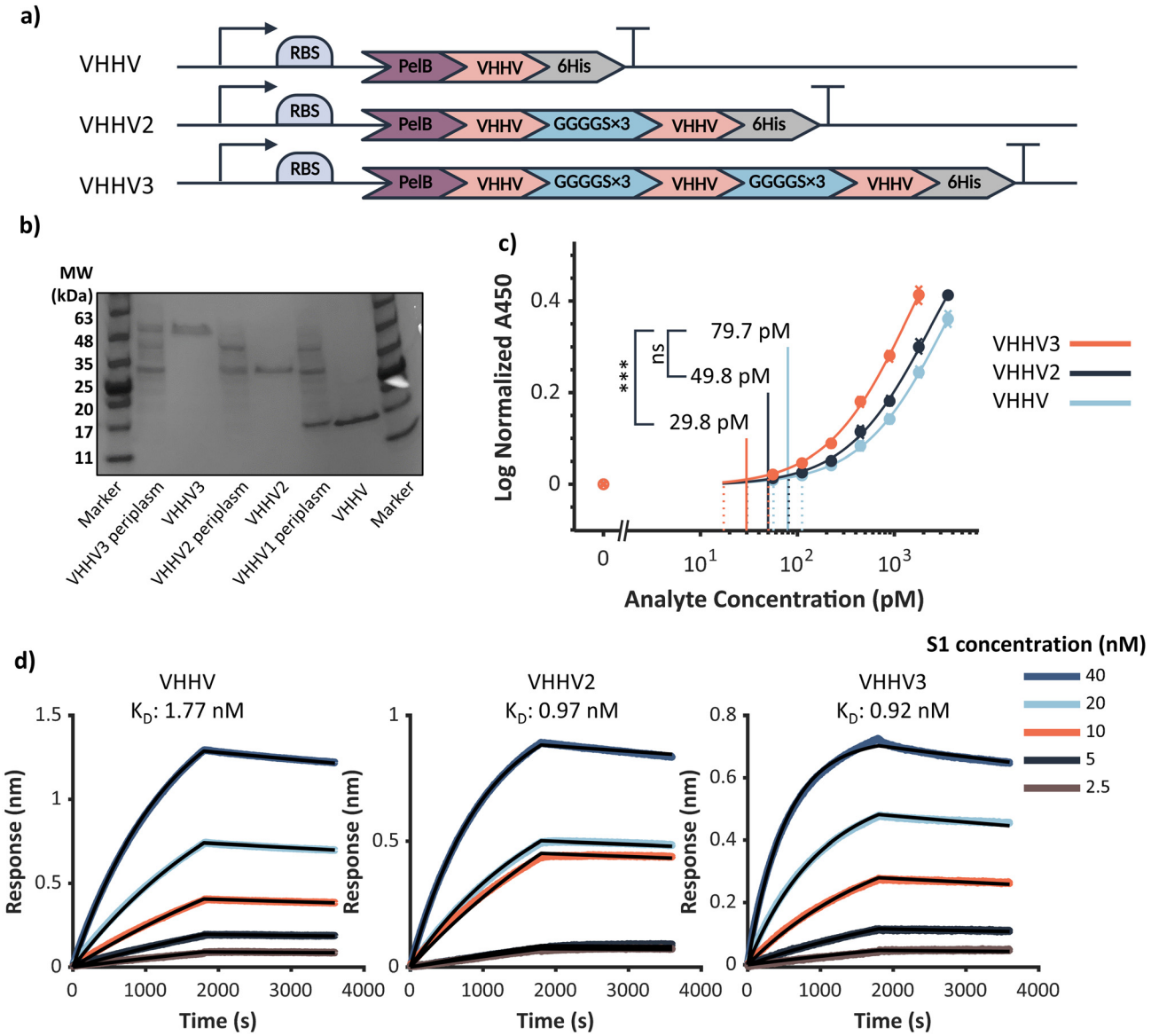

Fig. 4 Multivalent nanobody characterisation. (a) Gene diagram of the monovalent and multivalent nanobodies. (b) Reducing SDS-PAGE, Lanes 1 and 8 contain the protein MW reference marker, lanes 2 and 3 contain the periplasm and purified fraction from the VHHV3 expression, 4 and 5 contain the periplasm and purified fraction of VHHV2, lanes 6 and 7 contain the periplasm and purified fraction from the expression of VHHV. While the bands appear to consistently migrate slightly faster than their expected molecular weights, this gel was used primarily for qualitative assessment. The exact MW of the proteins were confirmed by Mass spectrometry (ESI Fig. 4–6†). (c) Limit of detection analysis from direct ELISA using biotinylated versions of nanobodies VHHV, VHHV2 and VHHV3 against the S1-Fc immobilised on the plate. Solid curves show the fitted Langmuir functions for VHHV, VHHV2 and VHHV3. Circles show the average of 3 replicates for each concentration ± the standard deviation of the mean. Vertical dashed lines show the 95% CI of the LoD calculation while solid vertical lines show the LoD. (d) Bio-layer interferometry of biotinylated VHHV, VHHV2 and VHHV3 against the SARS-CoV-2 S1-His antigen.

loads ranging from 1 to 4 biotins per nanobody, with the majority presenting 2 biotins (ESI Fig. 5–7†).

Nanobodies bearing double and triple valency exhibited a modest increase in binding affinity when compared to the monomeric form of VHHV. This is indicated by a decrease in the dissociation constant (k_D) from 1.77 ± 0.01 nM for VHHV to 0.97 ± 0.01 nM for VHHV2 and 0.92 ± 0.01 nM for VHHV3 (Fig. 4d). This modest improvement in affinity is consistent with previous findings by Koenig *et al.*, who reported a k_D of 8.92 nM for monovalent VHHV and 2.58 nM for the divalent form. While our values are lower, this could be attributed to differences in assay setup. Koenig *et al.* used an SPR system with immobilised antigens, whereas we used a BLI system with immobilised nanobodies.[33]

Direct ELISA was also performed with a flipped configuration, immobilising Fc-tagged S1 antigen on the solid phase and allowing nanobody constructs to bind from the solution. This direct ELISA format enabled a free configuration of the multimeric nanobodies, ensuring a fair comparison by minimising any potential impact on the LoD that might arise from differences in immobilisation between monovalent, divalent and trivalent nanobody constructs. Chemically biotinylated nanobodies served as detection reagents for signal generation. A significantly improved LoD was measured for VHHV3 at 29.8 pM (17.4–50.3 pM, 95% CI) when compared to VHHV's LoD of 79.7 pM (56.6–111.7 pM, 95% CI, p = 0.0034). A similar, though statistically non-significant, LoD decrease was observed for VHHV2 (49.8 pM, 30.1–81.5 pM, 95% CI, p = 0.13).

Multivalent VHHV physisorption

Multimeric nanobodies were physisorbed to AuNPs at a molar excess of 3200 nanobodies per gold nanoparticle, matching previous experiments. The effect of pH on bioconjugation was tested by conjugating at a range of pH conditions (pH 5.0–9.5) and monitoring the aggregation index (Fig. 5a). As anticipated, due to the similar IEPs of VHHV (6.70), VHHV2 (6.66) and VHHV3 (6.70) comparable aggregation index values were observed as a function of pH following physisorption. Nanoparticle stability was maintained during conjugation at pH greater than 6.0 for VHHV2 and VHHV3, and pH greater than 6.5 for VHHV. However, the addition of salt rapidly compromised the stability of VHHV2 bioconjugates across all pH

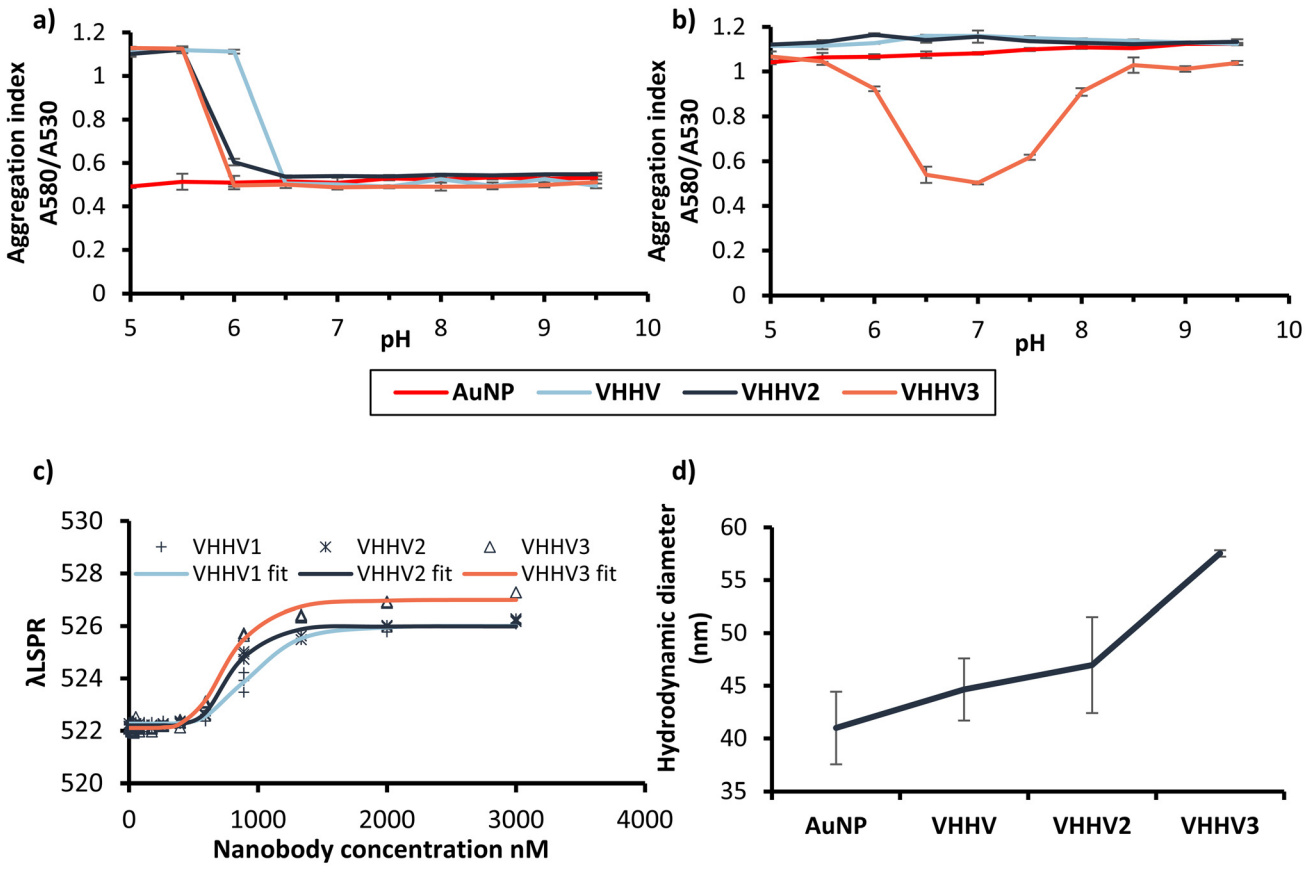

Fig. 5 AuNP adsorption characteristics of VHHV, VHHV2, and VHHV3. Aggregation index of VHHV, VHHV2 and VHHV3 bioconjugates before (a) and after (b) the addition of 400 mM NaCl. (c) Adsorption isotherm plots based on the plasmon peak shift for each bioconjugate. Solid lines represent the fitted Langmuir equation (eqn (1), Materials and methods), symbols show the individual data points for each nanobody. Extraction of the plasmon peaks and demonstration of the peak shift for each nanobody bioconjugates is shown in ESI Fig. 9.† (d) D_h for VHHV, VHHV2 and VHHV3 bioconjugates determined by DLS.

values, mirroring the behaviour of VHHV (Fig. 5b). This is not improved at higher nanobody concentrations for VHHV2 (ESI Fig. 8a†). This contrasts with the dimerised form of the disulfide-bridged VHHV-Cys, which retained some nanoparticle stability. While VHHV2 and dimerised VHHV-Cys nanobodies have similar molecular weights, they exhibit linkers with distinctly different lengths and flexibility. We hypothesise that the differences in linker flexibility (flexible in VHHV2, rigid in dimerised VHHV-Cys) and nanobody orientation (C-termini interfacing in the dimer) could lead to distinct approaches, binding mechanisms, and ultimately different protein structures upon adsorption to the AuNP surface, impacting the resulting bioconjugate stability.

In contrast to the low stability of VHHV and VHHV2 bioconjugates at elevated ionic strength, VHHV3 exhibited a stable region between pH 6.5 and 7.5 (Fig. 5b). The presence of an additional nanobody on VHHV3 correlated with enhanced nanoparticle protection against aggregation indicating improved colloidal stability likely due to differences in local charge and structure. Increasing the molar ratio of VHHV3 : AuNP to 6400 : 1 resulted in a similar aggregation index as a function of pH, suggesting that maximum coverage is achieved at or before 3200 VHHV3 nanobodies per nanoparticle (ESI Fig. 8b†). This protection against salt-induced aggregation also highlights the importance of balanced protein electrostatics. At pH values above 7.5, negatively charged proteins repel the negatively charged nanoparticles during conjugation, leaving them less effectively decorated, and vulnerable to salt-induced aggregation. Conversely, at pH values below 6.5, strongly positively charged VHHV3 proteins cross-link AuNPs, leading to aggregation. Therefore, a pH range between 6.5 and 7.5 provides an optimal environment where a protective protein layer shields the nanoparticle surface from salt-induced aggregation, without causing protein-mediated cross-linking.

Adsorption isotherms can be used to evaluate the adsorption characteristics of a protein to a surface.[42] The adsorption isotherm of each nanobody was calculated by monitoring the plasmon peak position with increasing nanobody concentration during bioconjugation (Fig. 5c). The dissociation constant determined reflects the rate at which the adsorbing protein is shifting the plasmon resonance. Notably, the equilibrium dissociation constant, K_d, was found to decrease with increasing nanobody valency (940.22, 789.43 and 759.21 nM for VHH1, VHH2 and VHH3 respectively). This likely reflects the larger size of these proteins requiring a reduced stoichiometry to fully modify the gold surface. Furthermore, VHHV3 exhibited a larger increase in the surface plasmon resonance peak wavelength (λSPR). This shift, linked to nanoparticle local refractive index changes, suggests a more pronounced change of the nanoparticle surface, potentially contributing to its superior salt stability.

DLS revealed a more pronounced increase in the D_h of VHHV3 of 57.5 nm (±0.3 nm) in comparison to VHHV and VHHV2 which yielded D_h of 44.7 nm (±3.4 nm) and 47.0 nm (±4.5 nm), respectively (Fig. 5d). The much larger increase in D_h for VHHV3 suggests that where nanobody domains may serve as anchor points, other nanobody domains likely extend outward from the surface. VHHV3, comprising 3 nanobodies linked with long flexible linkers, might be expected to exhibit more diverse conformations on approach and attachment to the nanoparticle surface compared to VHHV2 and VHHV. These may lead to more complex and sterically hindered interfaces that act to increase D_h. Given the adsorbed protein layer is on average, significantly thicker than the largest dimension of VHHV1, this could increase the likelihood of tethered, flexible nanobody domains being pendant from the surface. This helps rationalise the increased stability observed for VHHV3, as these extended domains may provide greater steric hindrance and a more protective protein layer. While antibodies and other proteins have been successful in preparing robust and stable bioconjugates, VHHV3 offers an appealing alternative. It benefits from the ease of production and development associated with nanobodies and provides a paratope-dense surface that could lead to improvements in sensing applications.

Nanobody bioconjugate LFA

The trivalent VHHV nanobody afforded a clear advantage in physisorbed bioconjugate stabilisation, however, both stability and function are critical for effective application. The performance of VHHV3, VHHV2 and VHHV nanobody AuNP bioconjugates were evaluated in LFA where the ability of the bioconjugates to withstand physiological ionic strengths, crowded protein environments and to demonstrate specific affinity interactions against the target protein could be assessed A simplified LFA format was engineered comprising the nanobody conjugated AuNPs, a biotinylated SARS-CoV-2 S1 analyte (S1-biotin) and a nitrocellulose membrane bearing polystreptavidin as a capture region (Fig. 6a and b). VHHV, VHHV2, and VHHV3 AuNP bioconjugates were prepared under identical optimised conditions and the conjugated proteins were blocked with BSA prior to purification. The binding of the bioconjugate to the antigen, followed by immobilisation of the immunocomplex at the test line, leads to bioconjugate accumulation and the formation of a red line, indicating a positive signal. Signal quantification can then be performed by image analysis of photos of the LFA strips. Dose–response functions are generated and the LoD is determined to provide a measure of the functionality of each bioconjugate. A large range of antigen concentrations (<3 logs) was used and tested in triplicate, ensuring the precise identification of the performance and reproducibility of each bioconjugate in detecting the antigen in this simplified assay format. Notably, VHHV and VHHV2 bioconjugates demonstrated weaker signal generation and significantly poorer limits of detection in the LFA format when compared to VHHV3 (Fig. 6c). While the LoD of VHHV3 bioconjugate was 257 pM (120–546 pM 95% CI), the corresponding values for VHHV and VHHV2 were 3630 pM (836–15 700 pM 95% CI $p < 0.005$) and 2650 pM (1530–4610 pM 95% CI $p < 0.005$) respectively. Importantly, the VHHV3-AuNP bioconjugate maintained its stability and functionality

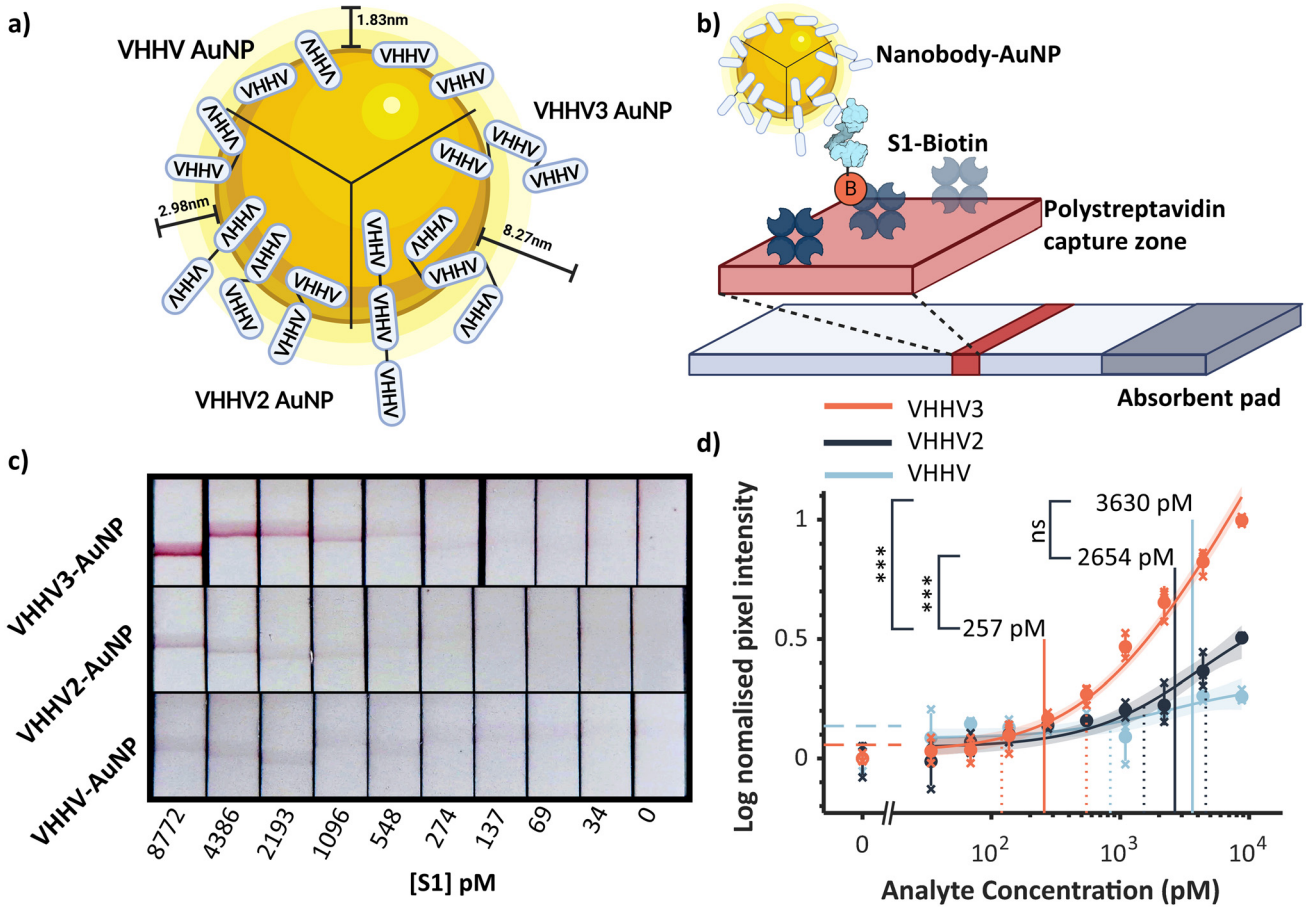

Fig. 6 Evaluation of nanobody bioconjugates in lateral flow assay (LFA) format. (a) Scheme indicating the 3 types of nanobody-AuNP bioconjugate and exemplar nanobody configurations. (b) Scheme of direct LFA showing capture of antigen bound immunocomplex and immobilisation to the polystreptavidin test-line *via* the chemically biotinylated antigen. (c) Images of LFA strips bearing test lines formed by bioconjugates immobilised at different antigen concentration. (d) Test line signal as a function of analyte concentration to establish LoD for each bioconjugate (n = 3), individual data points and their average is displayed as crosses and solid circles respectively ± the standard deviation of the mean. Solid curves show the fitted Langmuir functions. Dashed lines show the 95% CI of the LoD calculation while solid vertical lines show the LoD.

throughout the LFA process, including BSA blocking and multiple wash steps. Although VHHV and VHHV2 did not completely withstand the salt-induced aggregation test, a modest signal was generated at very high antigen concentrations following the completion of the bioconjugate preparation process, indicating some residual bioconjugate functionality. However, comparing the signal profiles, VHHV3-AuNP produced significantly more signal in comparison to VHHV2-AuNP and VHHV-AuNP (ESI Fig. 9b†). Notably, VHHV-AuNP retained some signal even at zero antigen concentration, indicative of non-specific binding and a further reduction in the signal-to-noise ratio. Interestingly, VHHV2-AuNP, despite showing similar instability to VHHV-AuNP, prior to BSA blocking, displayed enhanced signal generation and signal-to-noise ratio, suggesting a relationship between nanobody length and LFA performance, even in the divalent form, potentially due to enhanced paratope display. Nevertheless, the test lines for VHHV-AuNP and VHHV2-AuNP displayed a bluish colour, indicative of nanoparticle aggregation, further highlighting the limitations of these constructs in LFA applications. The superior performance of VHHV3-AuNP likely reflects its enhanced nanoparticle stability and the monodispersed nature of the bioconjugates, leading to a greater availability of functional binding sites during assay operation. In addition, the presentation of nanobodies further from the AuNP surface, as indicated by the protein layer thickness determined by DLS, could indicate an increased proportion of nanobody paratopes presented appropriately for target interaction.[43] Furthermore, VHHV3 not only demonstrates significantly lower LoD but also a much greater dynamic range.

Evaluation of resilience of VHHV3-AuNP bioconjugates to storage conditions

VHHV3 bioconjugates have been shown to accommodate the elevated ionic strengths associated with physiological conditions in a LFA and the presence of high concentrations of BSA. However, LFAs typically require the bioconjugates to be in a desiccated format for improved storage and simplicity which

is critical for future sensing applications. To assess the stability of our VHHV3-AuNP bioconjugates towards harsher storage conditions, their function in LFA was measured using bioconjugates that were either used as prepared, freeze–thawed from −80 °C, or freeze-dried prior to performing an S1-biotin antigen dose–response assay. While the freeze–thawed particles were suspended in the original running buffer consisting of 1% w/v BSA in 1× phosphate buffered saline (PBS) and 0.05% w/v Tween-20, the nanoparticles destined for lyophilisation were supplemented with 10% w/v sucrose for cryopreservation. Initially, bioconjugates frozen overnight at −80 °C in were found to maintain their analytical sensitivity, LoD of 343 pM (235–500 pM 95% CI), when compared to unprocessed VHHV3 bioconjugates, LoD of 257 pM (120–546 pM 95% CI), showing no significant change ($p > 0.05$, Fig. 7). Lyophilised bioconjugates, reconstituted with distilled water, also exhibited preservation of functionality presenting a LoD of 251 pM (163–385 pM 95% CI) which was not significantly different compared to the LoD of the unprocessed VHHV3 bioconjugate ($p > 0.05$). These findings demonstrate that our nanobody-AuNP bioconjugates retain near-complete functionality even after freeze-drying and reconstitution, a highly promising result for LFA applications. While the LoDs of the stored formats are not significantly different, the slight increase in LoD and decrease in signal intensity in the freeze–thawed bioconjugates may indicate further optimisation could improve the reconstitution of the bioconjugates.[21,32] During the freeze and lyophilisation process the nanoparticles are exposed to a dramatic increase in nanoparticle concentration and increase in the ionic strength of the solution due to ice formation and solute exclusion.[44] The resilience of VHHV3 bioconjugates to these harsh conditions highlights the potential of this construct for applications that demand stability and functionality during processing and storage, such as in LFAs.

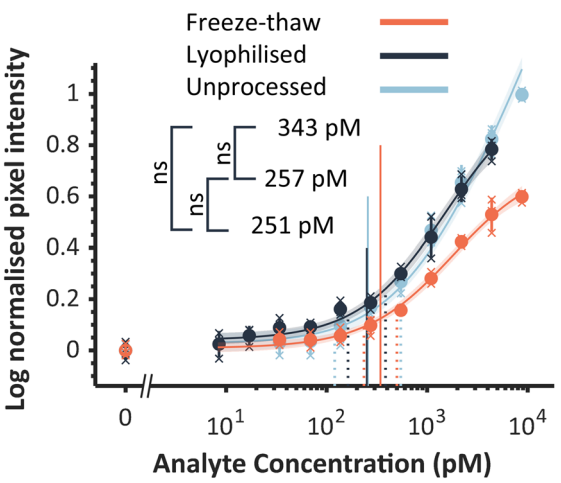

Fig. 7 LFA dose response of VHHV3 bioconjugates following freeze-thawing or lyophilisation. LoD analysis of the maximum signal for each S1-biotin concentration using a Langmuir fit. Shaded region around each fit shows the 95% CI of the fit ($n = 3$), individual data points and their average is displayed as crosses and solid circles respectively ± the standard deviation of the mean. Dashed lines show the 95% CI of the LoD calculation while solid vertical lines show the LoD.

Conclusions

In this study, we demonstrate a tractable route towards engineering nanobodies that effectively stabilise AuNP bioconjugates generated *via* physisorption. Leveraging efficient bacterial expression and a one-step physisorption process for bioconjugation, we identified how the use of a trivalent nanobody enables the generation of stable and functional AuNP bioconjugates for LFA applications. The physisorption of monovalent nanobodies, even in the presence of cysteine mutations fails to provide a protein layer capable of yielding bioconjugates that exhibit stability during initial physisorption procedures. Elevated ionic strength conditions resulted in instability for all the monomeric nanobody constructs tested, falling short of the requirements for biosensing applications. This is particularly important for immunoassays where the particles must resist exposure to elevated osmolality, high protein levels, and drying processes for storage. Increasing the molecular weight of the nanobody through engineering divalent and trivalent nanobodies, linked *via* flexible linker sequences, not only afforded salt tolerant AuNP bioconjugates but, in the case of the trivalent AuNP-bioconjugate, enabled the detection of pM concentrations of SARS-CoV-2 S1 protein in a $\frac{1}{2}$ dipstick model LFA format following freeze drying. This effective retention of stability and function allows for reconsideration of nanobody physisorption as a simple route for bioconjugate preparation for LFAs. In particular, the work opens new avenues for the development of point-of-care diagnostics that build from the understanding developed here using the model S1 system, applied to diagnostically relevant biomarkers for clinical applications.

Materials and methods

Generation of nanobodies

pET26b plasmids coding for the monovalent, and multivalent nanobodies were synthesised by GenScript. The amino acid sequences are listed in the ESI (Table 1).† Briefly, nanobody sequences were fused with an N-terminal PelB signal sequence and a C-terminal hexahistidine sequence for periplasmic production and hexahistidine affinity purification, respectively. Starter cultures were prepared by inoculating a colony of BL21 (DE3) cells transformed with plasmids coding for the nanobodies in 10 mL of LB media containing kanamycin (50 μg mL^{-1}, Gibco) and cultured at 37 °C overnight shaken at 250 rpm. The starter culture was then used to inoculate a 2 L shake flask containing 400 mL of LB media supplemented with kanamycin and then incubated at 37 °C, shaken at 250 rpm until the optical density at 600 nm reached 0.7. Expression of the constructs was induced with 1 mM of Isopropyl β-D-1-thiogalactopyranoside and incubated overnight at 25 °C shaken at 250

rpm. Cells were collected by centrifugation at 10 000*g* for 15 minutes. Periplasmic extraction was performed by resuspending the cells in 15 mL of TES (200 mM Tris HCl, 0.5 mM EDTA and 500 mM Sucrose, pH8) per L of culture and incubation for 2 hours on ice. Osmotic shock was performed by a 3-fold dilution with distilled water and incubation on ice for 1 hour. Cells were centrifuged for 30 min at 9000*g* and the supernatant was collected as the periplasmic extract. Nanobodies were separated from the periplasmic extract by Ni-NTA chromatography using a 1 mL His-trap HP column (Cytiva) by passing the sample through the column equilibrated in binding buffer (20 mM sodium phosphate, 500 mM NaCl, 30 mM imidazole, pH 7.4) and eluded from the column using elution buffer (20 mM sodium phosphate, 500 mM NaCl, 500 mM imidazole, pH 7.4). The elution fraction was buffer exchanged into PBS and concentrated using a protein Centrifugal Filter (Amicon, 3 kDa MWCO). Purity was evaluated using a 4–20% gradient SDS-PAGE (BIO-RAD) and visualised using Coomassie stain (Abcam).

Aggregation assays of AuNP bioconjugates

Nanobody physisorption studies were performed by mixing 5 μL of 100 mM buffer (pH 5.0–6.5 MES – Sigma, pH 7.0–8.5 HEPES – Sigma, 9.0–9.5 Borate – Fischer Chemical) with 5 μL of nanobody solution (3.6 μM) in a 384-well protein low binding plate (Greiner). 40 μL of 40 nm AuNPs (Nanocomposix) at OD 1.25 (Absorbance at 525 nm) were added to each well and mixed thoroughly. The plate was incubated for 1 h at room temperature. Absorbance measurements at 530 and 580 nm and absorption spectra (400 nm to 750 nm, 1 nm steps) were collected using the SpectraMax i3 (Molecular devices). Salt induced aggregation was performed by the addition of 50 μL of 800 mM NaCl. The plate was left to stand for 5 minutes and the absorbance measurements at 530 and 580 nm were recorded.

Cys mutant reduction reaction

VHHV nanobodies containing a free Cys on the N-terminus or C-terminus are denoted as Cys-VHHV and VHHV-Cys respectively. Cys bearing nanobodies were either used without reduction or with reduction. Reduced versions of the nanobodies are denoted with lower case r (for example, rCys-VHHV). The reduction reaction was carried out by mixing 10 mM TCEP–HCL with up to 100 μg mL^{-1} of nanobody and incubated for 5 minutes at RT. TCEP–HCl was removed from the reaction using Zeba Spin Desalting Columns (7 kDa MWCO, Thermo Fisher Scientific). Reduction to monomers was observed using a non-reducing SDS-PAGE. The integrity of the internal disulfide bridge was investigated by reacting the reduced protein with *N*-methylmaleimide and characterised using mass spectrometry (ESI Fig. 4†).

Nanoparticle size measurements

Dynamic light scattering (DLS) was performed to determine size of AuNP and AuNP bioconjugates using the Litesizer DLS 500 (Anton Paar). Measurements were taken at 90° detection angle at 25 °C using a disposable cuvette. Measurements were taken at AuNP concentration at OD 1.

Biotinylation reaction of proteins

Nanobodies and the S1 protein were biotinylated using the amine reactive NHS-PEG_{12}-Biotin (20-fold excess linker to protein). NHS-PEG_{12}-Biotin (Thermo) was diluted in DMSO (Sigma) immediately before use. NHS-PEG_{12}-Biotin was added to the protein mixture and incubated for 1 h at room temperature on the thermal shaker shaken at 650 rpm. Biotinylated proteins were passed through a ZebaSpin desalting column that was pre equilibrated with PBS (pH 7.4, Sigma) to remove the unreacted biotinylation reagent and elute in PBS. Final protein concentration was measured using a NanoDrop One (Thermo Fisher).

Quantification of nanobody binding constants

Nanobody binding constants were measured by Bio-layer interferometry (BLI) using the ForteBio Octet RED96 (Molecular Devices). Briefly, nanobodies were biotinylated using NHS-PEG12-Biotin in a 5 : 1 biotin to nanobody ratio. Unreacted biotin was removed using a ZebaSpin desalting column. Streptavidin functionalised sensors (Sartorius) were hydrated in Kinetics buffer (Sartorius) before being placed in fresh Kinetics buffer for a 5 minute baseline reading. Biotinylated nanobodies were loaded to the sensor at 1 μg mL^{-1} diluted in Kinetics buffer for 15 minutes. Sensors were then placed in kinetics buffer for a baseline step for equilibration for 10 minutes. Association step was performed by placing sensors in different concentrations of S1 (Abcam, His-tagged, 80, 40, 20, 10, 5, 2.5, 1.25, 0 nM) for 30 minutes. The dissociation step was performed by placing the sensors in Kinetics buffer for 30 minutes. Analysis and determination of the affinity constants was performed using the ForteBio Data Analysis 8.2 software. The antigen concentrations that provided the highest R squared value across all experiments were selected for the fitting.

Cys mutant analytical performance

VHHV and Reduced versions of Cys-VHHV and VHHV-Cys were used to coat the surface of Nunc maxisorb 96 well plates (Thermo) at 100 nM in PBS and incubated for 2 h at room temperature. The plate was washed 3 times with washing buffer (PBS and 0.05% v/v Tween-20, pH 7.4). The plate was then blocked with blocking buffer (3% w/v BSA, PBS and 0.05% v/v Tween-20) for 1 h and washed 3 times with washing buffer. Biotinylated S1 in blocking buffer was added to each well at different concentrations (1000, 333, 111, 37.0, 12.3, 4.1, 1.37, 0 ng ml^{-1}) and incubated at RT for 1 h. The plate was washed 5 times before adding horse radish peroxidase conjugated streptavidin (HRP-SA) (1 : 200 in blocking buffer) and incubating for 1 h. The plate was washed 5 times before adding TMB one-step substrate and left to develop signal for 5 minutes before adding 2 M H_2SO_4. Absorbance measurements at 450 nm were collected using the SpectraMax i3.

Multivalent nanobody ELISA

Nunc maxisorb 96 well plates were coated with S1-Fc antigen (Abcam, ab272105, PBS) at different concentrations (500, 250, 125, 62.5, 31.25, 15.6, 7.81, 0 ng mL^{-1}) for 1 h at room temperature. The plate was washed 3 times with washing buffer (PBS and 0.05% v/v Tween-20, pH 7.4) before being blocked with blocking buffer (3% w/v BSA, PBS and 0.05% v/v Tween-20, pH 7.4) for 1 h. The plate was washed 3 times with washing buffer before adding biotinylated nanobodies at 1 μg ml^{-1} in blocking buffer. Biotinylation ratio was confirmed using mass spectrometry (ESI Fig. 5–7†). The detection steps were performed as previously described.

Adsorption isotherm

5 μL of mono-, di- or trivalent VHHV was mixed with 5 μL of 100 mM HEPES buffer pH 7.0 in a 384-well plate. 40 μL of 40 nm AuNPs OD1.25 (A525) were added to the plate and mixed thoroughly before incubating for 1 h at room temperature. The final nanobody concentrations ranged from 3000 to 15.4 ng mL^{-1} using a 1.5-fold serial dilution. UV-Vis spectra were collected using the CLARIOstar Plus plate reader (BMG LABTECH, 220–1000 nm, 1 nm steps). The precise wavelength of the peak of the surface plasmon resonance (λSPR) peak was determined by fitting a Gaussian function to the plasmon peak from 500 nm to 550 nm and determining the maximum point by interpolation using a 0.05 nm precision (ESI Fig. 10†). The λSPR was plotted against concentration and best fitted to the hill equation (eqn (1)) where $\lambda SPR_{initial}$ is the λSPR of the bare gold nanoparticle, K_d is the dissociation constant of the interaction:

$$\lambda SPR = \lambda SPR_{initital} + \frac{\Delta\lambda SPR_{max}[\text{nanobody}]^n}{K_d^n + [\text{nanobody}]^n} \quad (1)$$

Nanobody-AuNP conjugation and LFA development

AuNP-VHHV3 bioconjugates were prepared by combining 100 μL of pH 7.5 HEPES buffer with 100 μL of VHHV3 (155 μg mL^{-1}) in 2 mL protein low-binding tubes. After briefly vortexing, 800 μL of 40 nm AuNPs (OD 1.25 at 525 nm) were added and incubated for 1 h on a thermal shaker at 650 rpm at room temperature. Bioconjugates were blocked by adding 1 mL of blocking buffer (1% w/v BSA, 0.05% v/v Tween-20 in PBS) and incubating for another hour. Bioconjugates were then centrifuged at 3500*g* for 10 minutes, the supernatant removed, and the pellet resuspended in blocking buffer. This washing process was repeated once, and the final AuNP-VHHV3 bioconjugate was adjusted to OD 2 at 525 nm. For LFA assembly, 100 mm × 20 mm SureWick absorbent pads (Millipore) were attached to 100 mm of FF80HP plus nitrocellulose membrane (Cytiva) using their adhesive backing. The assembled cards were cut to 100 mm, and the bottom adhesive was removed with a guillotine cutter. Test lines were printed using a Biodot AD1520 dispenser (dispensing rate of 1 μL cm^{-1}) with polystreptavidin (BioTez, 1 mg ml^{-1} in purified water) positioned 10 mm below the absorbent pad. After printing, membranes were dried at 37 °C in the oven for 1 hour. Finally, 3 mm half-stick LFAs were cut using ZQ2002 Strip Cutter (Kinbio).

Lateral flow immunoassay

To perform the immunoassay, 10 μL of AuNP-VHHV3 bioconjugates (OD 2 at 525 nm) were added to a protein low-binding 96-well plate (Greiner). Dilution series of the biotinylated S1-His antigen were prepared in blocking buffer (concentrations ranging from 2000 ng ml^{-1} to 0 ng ml^{-1}) and added 5 μL of each dilution to the corresponding well containing the bioconjugates. After mixing well and a 5 minute incubation at room temperature, half-stick LFAs were inserted into each well. The assays were allowed to fully wick and air dry. Images of the LFAs were captured using a Canon PowerShot G15 camera in a light box, and an in-house developed MATLAB software was used to analyse the maximum intensity of each assay's test line. Briefly, sections from the lateral flow images containing the test lines were manually selected, cropped, separated to the green channel and the image was reduced to one dimension by averaging along the lateral axis. The background was determined by a 100-pixel area away from the testline and subtracted from the inverted trace. Signal is quantified as the maximum intensity point along the trace.

Nanobody bioconjugate storage

AuNP bioconjugates for storage stability studies were prepared as previously described. 10 μL aliquots of bioconjugate were dispensed into a 96-well plate, covered with adhesive film, and frozen overnight at −80 °C. For analysis, bioconjugates were thawed at room temperature for 30 minutes with shaking. Antigen dilutions were added directly to the 96-well plate, and LFAs were performed as previously described. For freeze-drying experiments, nanoparticles were suspended in running buffer containing 10% sucrose before dispensing into a 96-well plate. The plate was covered with adhesive film and frozen overnight at −80 °C. Frozen bioconjugates were then lyophilized (freeze-dried) overnight. To reconstitute, 10 μL of deionized water was added to each well containing freeze-dried bioconjugates and shaken on a plate shaker at 650 rpm for 10 minutes. Antigen was added directly to the same plate and incubated for 5 minutes before performing the LFAs.

Limit of detection analysis

Limit of detection analysis and statistical analysis of the dose–response data of the Cys mutant analytical performance ELISA, the multivalent nanobody ELISA and nanobody-AuNP bioconjugate LFAs was performed using the software developed by Miller *et al.*, based on methods developed by Holstein *et al.* by fitting a Langmuir function to the dose-response data.[45,46]

Author contributions

J.P.A., S.F., and M.R.T. conceived the research and led the study. J.P.A., C.H. and M.R.T. designed the majority of experi-

ments. J.P.A. conducted the majority of experiments. H.Z. & J.P.A. conducted SDS-PAGE and BLI for the protein characterisation of the multivalent nanobodies. J.P.A., C.H., V.C., S.F. and M.R.T. performed formal analysis of the data. J.P.A. and M.R.T. drafted the manuscript. All authors revised and reviewed the manuscript.

Data availability

Data for this article are available at the UCL Research Data Repository at **https://doi.org/10.5522/04/27161412.v1**.

Conflicts of interest

There are no conflicts to declare.

Acknowledgements

This work was funded by the EPSRC, supporting J. P. A. (EP/T517793/1) and C. H. (EP/T517793/1). The authors also acknowledge the support of the i-sense: EPSRC IRC in Agile Early Warning Sensing Systems for Infectious Diseases and Antimicrobial Resistance grant (EP/R00529X/1). The authors would also like to acknowledge the UCL Chemistry Mass Spectrometry Facility (Dr K. Karu). M. T. and S. F. acknowledge support from the DHSC/EPSRC funded VaxHub Global project (EP/Y530542/1).

References

1 J. Budd, B. S. Miller, N. E. Weckman, D. Cherkaoui, D. Huang, A. T. Decruz, N. Fongwen, G.-R. Han, M. Broto, C. S. Estcourt, J. Gibbs, D. Pillay, P. Sonnenberg, R. Meurant, M. R. Thomas, N. Keegan, M. M. Stevens, E. Nastouli, E. J. Topol, A. M. Johnson, M. Shahmanesh, A. Ozcan, J. J. Collins, M. Fernandez-Suarez, B. Rodriguez, R. W. Peeling and R. A. McKendry, *Nat. Rev. Bioeng.*, 2023, **1**, 13–31.

2 J. Stokes, A. J. Turner, L. Anselmi, M. Morciano and T. Hone, *BMC Public Health*, 2022, **22**, 1–14.

3 S. Moore, E. M. Hill, M. J. Tildesley, L. Dyson and M. J. Keeling, *Lancet Infect. Dis.*, 2021, **21**, 793–802.

4 D. Gasperino, T. Baughman, H. V. Hsieh, D. Bell and B. H. Weigl, *Annu. Rev. Anal. Chem.*, 2018, **11**, 219–244.

5 C. E. Z. Chan, A. H. Y. Chan, A. P. C. Lim and B. J. Hanson, *J. Immunol. Methods*, 2011, **373**, 79–88.

6 E. R. Gray, J. C. Brookes, C. Caillat, V. Turbé, B. L. J. Webb, L. A. Granger, B. S. Miller, L. E. McCoy, M. El Khattabi, C. T. Verrips, R. A. Weiss, D. M. Duffy, W. Weissenhorn and R. A. McKendry, *ACS Infect. Dis.*, 2017, **3**, 479–491.

7 I. Zimmermann, P. Egloff, C. A. J. Hutter, B. T. Kuhn, P. Bräuer, S. Newstead, R. J. P. Dawson, E. R. Geertsma and M. A. Seeger, *Nat. Protoc.*, 2020, **15**, 1707–1741.

8 M. Schoof, B. Faust, R. A. Saunders, S. Sangwan, V. Rezelj, N. Hoppe, M. Boone, C. B. Billesbølle, C. Puchades, C. M. Azumaya, H. T. Kratochvil, M. Zimanyi, I. Deshpande, J. Liang, S. Dickinson, H. C. Nguyen, C. M. Chio, G. E. Merz, M. C. Thompson, D. Diwanji, K. Schaefer, A. A. Anand, N. Dobzinski, B. S. Zha, C. R. Simoneau, K. Leon, K. M. White, U. S. Chio, M. Gupta, M. Jin, F. Li, Y. Liu, K. Zhang, D. Bulkley, M. Sun, A. M. Smith, A. N. Rizo, F. Moss, A. F. Brilot, S. Pourmal, R. Trenker, T. Pospiech, S. Gupta, B. Barsi-Rhyne, V. Belyy, A. W. Barile-Hill, S. Nock, Y. Liu, N. J. Krogan, C. Y. Ralston, D. L. Swaney, A. García-Sastre, M. Ott, M. Vignuzzi, P. Walter, A. Manglik, C. M. Azumaya, C. Puchades, M. Sun, J. R. Braxton, A. F. Brilot, M. Gupta, F. Li, K. E. Lopez, A. Melo, G. E. Merz, F. Moss, J. Paulino, T. H. Pospiech, S. Pourmal, A. N. Rizo, A. M. Smith, P. V. Thomas, F. Wang, Z. Yu, M. S. Dickinson, H. C. Nguyen, D. Asarnow, M. G. Campbell, C. M. Chio, U. S. Chio, D. Diwanji, B. Faust, M. Gupta, N. Hoppe, M. Jin, J. Li, Y. Liu, G. E. Merz, S. Sangwan, T. K. M. Tsui, R. Trenker, D. Trinidad, E. Tse, K. Zhang, F. Zhou, N. Herrera, H. T. Kratochvil, U. Schulze-Gahmen, M. C. Thompson, I. D. Young, J. Biel, I. Deshpande, X. Liu, C. B. Billesbølle, C. Nowotny, A. M. Smith, J. Zhao, A. Bowen, N. Hoppe, Y.-L. Li, P. Nguyen, M. Safari, K. Schaefer, N. Whitis, M. Moritz, T. W. Owens, A. Diallo, K. Kim, J. K. Peters, E. W. Titus, J. Chen, L. Doan, S. Flores, V. L. Lam, Y. Li, M. Lo, A. C. Thwin, S. Wankowicz, Y. Zhang, D. Bulkley, A. Joves, A. Joves, L. McKay, M. Tabios, O. S. Rosenberg, K. A. Verba, D. A. Agard, Y. Cheng, J. S. Fraser, A. Frost, N. Jura, T. Kortemme, N. J. Krogan, A. Manglik, D. R. Southworth and R. M. Stroud, *Science*, 2020, **370**, 1473–1479.

9 N. R. Bennett, J. L. Watson, R. J. Ragotte, A. J. Borst, D. L. See, C. Weidle, R. Biswas, E. L. Shrock, P. J. Y. Leung, B. Huang, I. Goreshnik, R. Ault, K. D. Carr, B. Singer, C. Criswell, D. Vafeados, M. G. Sanchez, H. M. Kim, S. V. Torres, S. Chan and D. Baker, *biorxiv*, 2024, preprint, **https://www.biorxiv.org/content/10.1101/2024.03.14.585103v1**.

10 R. Vazquez-Lombardi, D. Nevoltris, A. Luthra, P. Schofield, C. Zimmermann and D. Christ, *Nat. Protoc.*, 2018, **13**, 99–117.

11 C. K. Kariuki and S. Magez, *Protein Expression Purif.*, 2021, **185**, 1–9.

12 E. Pardon, T. Laeremans, S. Triest, S. G. F. Rasmussen, A. Wohlkönig, A. Ruf, S. Muyldermans, W. G. J. Hol, B. K. Kobilka and J. Steyaert, *Nat. Protoc.*, 2014, **9**, 674–693.

13 E. A. Bastos-Soares, R. M. O. Sousa, A. F. Gómez, J. Alfonso, A. M. Kayano, F. B. Zanchi, M. E. Funes-Huacca, R. G. Stábeli, A. M. Soares, S. S. Pereira and C. F. C. Fernandes, *Int. J. Biol. Macromol.*, 2020, **165**, 2244–2252.

14 R. T. Busch, F. Karim, J. Weis, Y. Sun, C. Zhao and E. S. Vasquez, *ACS Omega*, 2019, **4**, 15269–15279.

15 O. Awotunde, S. Okyem, R. Chikoti and J. D. Driskell, *Langmuir*, 2020, **36**, 9241–9249.
16 D. Bartczak and A. G. Kanaras, *Langmuir*, 2011, **27**, 10119–10123.
17 B. Van De Broek, N. Devoogdt, A. Dhollander, H. L. Gijs, K. Jans, L. Lagae, S. Muyldermans, G. Maes and G. Borghs, *ACS Nano*, 2011, **5**, 4319–4328.
18 J. E. Pinto Torres, J. Goossens, J. Ding, Z. Li, S. Lu, D. Vertommen, P. Naniima, R. Chen, S. Muyldermans, Y. G.-J. Sterckx and S. Magez, *Sci. Rep.*, 2018, **8**, 1–15.
19 J. P. Salvador, N. Vasylieva, I. Gonzalez-Garcia, M. Jin, R. Caster, J. B. Siegel and B. D. Hammock, *ACS Food Sci. Technol.*, 2022, **2**, 1276–1282.
20 S. Y. Doerflinger, J. Tabatabai, P. Schnitzler, C. Farah, S. Rameil, P. Sander, A. Koromyslova and G. S. Hansman, *mSphere*, 2016, **1**, 1–16.
21 C. N. Loynachan, M. R. Thomas, E. R. Gray, D. A. Richards, J. Kim, B. S. Miller, J. C. Brookes, S. Agarwal, V. Chudasama, R. A. McKendry and M. M. Stevens, *ACS Nano*, 2018, **12**, 279–288.
22 G. Gonzalez-Sapienza, M. A. Rossotti and S. Tabares-da Rosa, *Front. Immunol.*, 2017, **8**, 1–12.
23 M. Kamel, S. Maher, H. El-Baz, F. Salah, O. Sayyouh and Z. Demerdash, *Trop. Med. Infect. Dis.*, 2022, **7**, 1–13.
24 Y. H. Lee, H. Medhi, X. Liu, I. H. Ha, K. T. Nam and H. Ploegh, *ACS Appl. Mater. Interfaces*, 2023, **15**, 59258–59268.
25 X. Wang, T. Sun, W. Shen, M. Liu, W. Liu, H. Zuo, Y. Zhang, L. Geng, W. Wang, C. Shao and J. Bai, *Sens. Actuators, B*, 2023, **394**, 1–11.
26 X. Chen, S. Kang, M. A. Ikbal, Z. Zhao, Y. Pan, J. Zuo, L. Gu and C. Wang, *Biosens. Bioelectron.*, 2022, **202**, 1–10.
27 G. P. Anderson, J. L. Liu, L. C. Shriver-Lake, D. Zabetakis, V. A. Sugiharto, H.-W. Chen, C.-R. Lee, G. N. Defang, S.-J. L. Wu, N. Venkateswaran and E. R. Goldman, *Anal. Chem.*, 2019, **91**, 9424–9429.
28 J. Goossens, H. Sein, S. Lu, M. Radwanska, S. Muyldermans, Y. G. J. Sterckx and S. Magez, *Anal. Methods*, 2017, **9**, 3430–3440.
29 T. Hattori, M. Umetsu, T. Nakanishi, S. Sawai, S. Kikuchi, R. Asano and I. Kumagai, *Bioconjugate Chem.*, 2012, **23**, 1934–1944.
30 G. P. Anderson, L. C. Shriver-Lake, J. L. Liu and E. R. Goldman, *Antibodies*, 2022, **11**, 1–10.
31 G. Ruiz, K. Tripathi, S. Okyem and J. D. Driskell, *Bioconjugate Chem.*, 2019, **30**, 1182–1191.
32 C. Parolo, A. Sena-Torralba, J. F. Bergua, E. Calucho, C. Fuentes-Chust, L. Hu, L. Rivas, R. Álvarez-Diduk, E. P. Nguyen, S. Cinti, D. Quesada-González and A. Merkoçi, *Nat. Protoc.*, 2020, **15**, 3788–3816.
33 P.-A. Koenig, H. Das, H. Liu, B. M. Kümmerer, F. N. Gohr, L.-M. Jenster, L. D. J. Schiffelers, Y. M. Tesfamariam, M. Uchima, J. D. Wuerth, K. Gatterdam, N. Ruetalo, M. H. Christensen, C. I. Fandrey, S. Normann, J. M. P. Tödtmann, S. Pritzl, L. Hanke, J. Boos, M. Yuan, X. Zhu, J. L. Schmid-Burgk, H. Kato, M. Schindler, I. A. Wilson, M. Geyer, K. U. Ludwig, B. M. Hällberg, N. C. Wu and F. I. Schmidt, *Science*, 2021, **371**, 1–15.
34 G. Bao, M. Tang, J. Zhao and X. Zhu, *EJNMMI Res.*, 2021, **11**, 1–13.
35 M. J. Pollitt, G. Buckton, R. Piper and S. Brocchini, *RSC Adv.*, 2015, **5**, 24521–24527.
36 J. S. Gebauer, M. Malissek, S. Simon, S. K. Knauer, M. Maskos, R. H. Stauber, W. Peukert and L. Treuel, *Langmuir*, 2012, **28**, 9673–9679.
37 S. Dominguez-Medina, L. Kisley, L. J. Tauzin, A. Hoggard, B. Shuang, A. S. D. S. Indrasekara, S. Chen, L. Y. Wang, P. J. Derry, A. Liopo, E. R. Zubarev, C. F. Landes and S. Link, *ACS Nano*, 2016, **10**, 2103–2112.
38 K. E. Woods, Y. R. Perera, M. B. Davidson, C. A. Wilks, D. K. Yadav and N. C. Fitzkee, *J. Phys. Chem. C*, 2016, **120**, 27944–27953.
39 A. Wang, K. Vangala, T. Vo, D. Zhang and N. C. Fitzkee, *J. Phys. Chem. C*, 2014, **118**, 8134–8142.
40 T. Pleiner, M. Bates, S. Trakhanov, C.-T. Lee, J. E. Schliep, H. Chug, M. Böhning, H. Stark, H. Urlaub and D. Görlich, *eLife*, 2015, **4**, 1–21.
41 M. Schoof, B. Faust, R. A. Saunders, S. Sangwan, V. Rezelj, N. Hoppe, M. Boone, C. B. Billesbølle, C. Puchades, C. M. Azumaya, H. T. Kratochvil, M. Zimanyi, I. Deshpande, J. Liang, S. Dickinson, H. C. Nguyen, C. M. Chio, G. E. Merz, M. C. Thompson, D. Diwanji, K. Schaefer, A. A. Anand, N. Dobzinski, B. S. Zha, C. R. Simoneau, K. Leon, K. M. White, U. S. Chio, M. Gupta, M. Jin, F. Li, Y. Liu, K. Zhang, D. Bulkley, M. Sun, A. M. Smith, A. N. Rizo, F. Moss, A. F. Brilot, S. Pourmal, R. Trenker, T. Pospiech, S. Gupta, B. Barsi-Rhyne, V. Belyy, A. W. Barile-Hill, S. Nock, Y. Liu, N. J. Krogan, C. Y. Ralston, D. L. Swaney, A. García-Sastre, M. Ott, M. Vignuzzi, P. Walter, A. Manglik, C. M. Azumaya, C. Puchades, M. Sun, J. R. Braxton, A. F. Brilot, M. Gupta, F. Li, K. E. Lopez, A. Melo, G. E. Merz, F. Moss, J. Paulino, T. H. Pospiech, S. Pourmal, A. N. Rizo, A. M. Smith, P. V. Thomas, F. Wang, Z. Yu, M. S. Dickinson, H. C. Nguyen, D. Asarnow, M. G. Campbell, C. M. Chio, U. S. Chio, D. Diwanji, B. Faust, M. Gupta, N. Hoppe, M. Jin, J. Li, Y. Liu, G. E. Merz, S. Sangwan, T. K. M. Tsui, R. Trenker, D. Trinidad, E. Tse, K. Zhang, F. Zhou, N. Herrera, H. T. Kratochvil, U. Schulze-Gahmen, M. C. Thompson, I. D. Young, J. Biel, I. Deshpande, X. Liu, C. B. Billesbølle, C. Nowotny, A. M. Smith, J. Zhao, A. Bowen, N. Hoppe, Y.-L. Li, P. Nguyen, M. Safari, K. Schaefer, N. Whitis, M. Moritz, T. W. Owens, A. Diallo, K. Kim, J. K. Peters, E. W. Titus, J. Chen, L. Doan, S. Flores, V. L. Lam, Y. Li, M. Lo, A. C. Thwin, S. Wankowicz, Y. Zhang, D. Bulkley, A. Joves, A. Joves, L. McKay, M. Tabios, O. S. Rosenberg, K. A. Verba, D. A. Agard, Y. Cheng, J. S. Fraser, A. Frost, N. Jura, T. Kortemme, N. J. Krogan, A. Manglik, D. R. Southworth and R. M. Stroud, *Science*, 2020, **370**, 1473–1479.
42 J. X. Xu, Md. S. Alom, R. Yadav and N. C. Fitzkee, *Nat. Commun.*, 2022, **13**, 1–11.

43 D. A. Richards, M. R. Thomas, P. A. Szijj, J. Foote, Y. Chen, J. C. F. Nogueira, V. Chudasama and M. M. Stevens, *Nanoscale*, 2021, **13**, 11921–11931.
44 A. M. Alkilany, S. R. Abulateefeh, K. K. Mills, A. I. Bani Yaseen, M. A. Hamaly, H. S. Alkhatib, K. M. Aiedeh and J. W. Stone, *Langmuir*, 2014, **30**, 13799–13808.
45 C. A. Holstein, M. Griffin, J. Hong and P. D. Sampson, *Anal. Chem.*, 2015, **87**, 9795–9801.
46 B. S. Miller, M. R. Thomas, M. Banner, J. Kim, Y. Chen, Q. Wei, D. K. Tseng, Z. S. Göröcs, A. Ozcan, M. M. Stevens and R. A. McKendry, *Biosens. Bioelectron.*, 2022, **207**, 114133.
47 E. Jurrus, D. Engel, K. Star, K. Monson, J. Brandi, L. E. Felberg, D. H. Brookes, L. Wilson, J. Chen, K. Liles, M. Chun, P. Li, D. W. Gohara, T. Dolinsky, R. Konecny, D. R. Koes, J. E. Nielsen, T. Head-Gordon, W. Geng, R. Krasny, G. W. Wei, M. J. Holst, J. A. McCammon and N. A. Baker, *Protein Sci.*, 2018, **27**, 112–128.
48 J. Jumper, R. Evans, A. Pritzel, T. Green, M. Figurnov, O. Ronneberger, K. Tunyasuvunakool, R. Bates, A. Žídek, A. Potapenko, A. Bridgland, C. Meyer, S. A. A. Kohl, A. J. Ballard, A. Cowie, B. Romera-Paredes, S. Nikolov, R. Jain, J. Adler, T. Back, S. Petersen, D. Reiman, E. Clancy, M. Zielinski, M. Steinegger, M. Pacholska, T. Berghammer, S. Bodenstein, D. Silver, O. Vinyals, A. W. Senior, K. Kavukcuoglu, P. Kohli and D. Hassabis, *Nature*, 2021, **596**, 583–589.
49 M. Mirdita, K. Schütze, Y. Moriwaki, L. Heo, S. Ovchinnikov and M. Steinegger, *Nat. Methods*, 2022, **19**, 679–682.